SCIENCE CHINA
Chemistry

•ARTICLES•

September 2024 Vol.67 No.9: 2949–2957
https://doi.org/10.1007/s11426-024-2125-5

Continuous Fe^{3+} releasing enabled complete reconstruction of Ni-based MOF for promoted water oxidation in industrial alkali

Zhaojian Wang[1†], Wei Zhang[1†], Wenzhong Huang[1†], Ruohan Yu[1,2], Changliang Chen[1], Liqiang Mai[1,3] & Liang Zhou[1,3*]

[1]*State Key Laboratory of Advanced Technology for Materials Synthesis and Processing, Wuhan University of Technology, Wuhan 430070, China;*
[2]*Sanya Science and Education Innovation Park, Wuhan University of Technology, Sanya 572000, China;*
[3]*Hubei Longzhong Laboratory, Wuhan University of Technology (Xiangyang Demonstration Zone), Xiangyang 441000, China*

Received April 10, 2024; accepted May 29, 2024; published online August 12, 2024

Most oxygen evolution reaction (OER) electrocatalysts show poor stability under industrial alkaline conditions (20–30 wt.% KOH). Therefore, it is essential to develop stable, efficient, and low-cost OER catalysts for industrial water electrolysis. Herein, we present a straightforward approach for the complete electrochemical reconstruction of Ni-BDC, a Ni-based metal-organic framework, for OER. This method involves the continuous release of Fe^{3+} from Fe foam counter electrode in a high-concentration (6.0 M, 25 wt.%) KOH solution. The continuously Fe^{3+} releasing not only realizes *in situ* Fe^{3+} doping, but also introduces abundant defects in the obtained catalyst during cyclic voltammetry activation, thereby accelerating the electrochemical reconstruction. The reconstructed OER catalyst (Fe-doped nickel hydroxide/oxyhydroxide nanosheets supported on Ni foam, Fe-$NiO_x(OH)_y$/NF) manifests a low overpotential of 217 mV at 10 mA cm^{-2} and 263 mV at 100 mA cm^{-2} in 1.0 M KOH. Noteworthy, the Fe-$NiO_x(OH)_y$/NF also demonstrates high stability in 30 wt.% KOH. This strategy of regulating the electrochemical reconstruction process sheds light on the construction of stable and efficient OER catalysts for industrial water electrolysis.

oxygen evolution reaction, industrial alkaline conditions, metal-organic framework, complete reconstruction

Citation: Wang Z, Zhang W, Huang W, Yu R, Chen C, Mai L, Zhou L. Continuous Fe^{3+} releasing enabled complete reconstruction of Ni-based MOF for promoted water oxidation in industrial alkali. *Sci China Chem*, 2024, 67: 2949–2957, https://doi.org/10.1007/s11426-024-2125-5

1 Introduction

With the continuous consumption of fossil energy, the exploration of renewable energy is imperative to solve the global issues of growing energy crisis and deteriorating ecological environment [1,2]. Electrochemical water splitting represents an attractive method for producing hydrogen from renewable energy [3]. Compared to hydrogen evolution reaction, the oxygen evolution reaction (OER) usually needs to overcome a large thermodynamic barrier to drive the reaction, which inevitably hinders the conversion efficiency of water splitting [4]. Therefore, developing efficient OER electrocatalysts is crucial to promote the reaction [5,6]. Noble metal-based catalysts, such as Ru- and Ir-based, have the most effective catalytic effect on OER [7,8]. However, noble metals are scarce and expensive. Thus, developing efficient alternative non-noble metal catalysts is necessary [9].

Transition-metal based catalysts, particularly NiFe-based catalysts, have demonstrated water oxidation activity comparable to that of noble metal electrocatalysts in alkaline media, making them a viable alternative [10,11]. The main

†These authors contributed equally to this work.
*Corresponding author (email: liangzhou@whut.edu.cn)

challenge of the NiFe-based OER catalysts is their usually poor stability. Recent studies [12,13] have indicated that most catalysts undergo a surface reconstruction process during OER, and the real active center is formed during the surface reconstruction [14]. The reconstruction of pre-catalysts has become an effective strategy for the preparation of highly efficient OER catalysts [15]. For example, Fang *et al*. [16] proposed a surface reconstruction method through anodic polarization to improve the OER performances of nickel-based perovskite hydroxide. Recent study [17] has identified that the oxyhydroxide generated on the reconstructed surface serves as the true active center for OER, and the *in situ* generated oxyhydroxide during surface reconstruction often exhibits better OER catalytic performance than the directly synthesized oxyhydroxide. As a result, the regulation of reconstruction is essential for the construction of high-performance OER catalysts [18]. For instance, Zhang *et al*. [19] proposed an F-doping method to regulate the surface reconstruction of $LaNi_{0.75}Fe_{0.25}O_3$ perovskite, resulting in an OER catalyst with a low overpotential. However, it remains challenging to regulate the reconstruction process precisely, as the catalysts obtained through reconstruction often deviate from the targets.

Ni-BDC, a Ni-based metal organic framework (MOF) with terephthalic acid (H_2BDC) ligand, is an ideal OER pre-catalyst due to the instability of MOF materials under electrochemical water oxidation conditions, which aids in triggering the reconstruction process [20]. However, the OER activity of catalyst through reconstruction of single-metal center MOF, such as Ni-BDC, is usually quite limited. Doping the single-metal center MOF with foreign metal elements has been demonstrated to be valuable in boosting its intrinsic catalytic activity through the synergistic effects between different metal elements [21]. In addition, the doping of foreign metal ions can lead to amorphization of the crystal structure of MOF due to the lattice mismatch, thereby accelerating the reconstruction.

Herein, we propose a continuous Fe^{3+} releasing enabled complete reconstruction strategy to construct high-performance OER catalysts (Fe-$NiO_x(OH)_y$/NF) using Ni-BDC supported on Ni foam as the precursor. The reconstruction of Ni-BDC/NF precursor is initiated by cyclic voltammetry (CV) activation in an industrial alkaline solution (6.0 M KOH). The *in situ* Fe^{3+} doping is realized though the CV induced continuous leaching of Fe^{3+} from the Fe foam counter electrode, which enables the complete reconstruction of Ni-BDC/NF. The obtained OER catalyst (Fe-$NiO_x(OH)_y$/NF) with low crystallinity manifests a low overpotential of 217 mV at 10 mA cm^{-2} and 263 mV at 100 mA cm^{-2} in 1.0 M KOH. The Fe-$NiO_x(OH)_y$/NF also demonstrates high stability in industrial alkaline solution (30 wt.% KOH) with a negligible activity decay of 0.09 mV h^{-1} (200 h at 100 mA cm^{-2}).

2 Experimental

2.1 Chemicals

$NiCl_2·6H_2O$ (98%, Sinopharm Chemical Reagent Co., Ltd, China), H_2BDC (99%, AladinReagent Co., Ltd, China), and KOH (95%, Aladin Reagent Co., Ltd, China) were purchased from commercial suppliers. Ni foam and Fe foam were purchased from Kunshan Guangjiayuan Electronics Co., Ltd.

2.2 Synthesis of Fe-$NiO_x(OH)_y$/NF

Firstly, the Fe foam was cleaned by acetone and 1.2 M HCl solution. The as-prepared Ni-BDC/NF, the cleaned Fe foam, and Hg/HgO electrode were employed as the working electrode, counter electrode, and reference electrode, respectively. The electrochemical three electrode system was used to prepare Fe-$NiO_x(OH)_y$/NF by CV with a scan rate of 100 mV s^{-1} in 6.0 M KOH solution in the potential window of −0.2–0.9 V *vs*. Hg/HgO (300 CV cycles). By controlling the CV cycle number, a series of samples can be obtained: Fe-$NiO_x(OH)_y$/NF-z (z = 0, 10, …, 300, 400). The corresponding powder collected from the Fe-$NiO_x(OH)_y$/NF-z is designated as Fe-$NiO_x(OH)_y$-z.

2.3 Electrochemical measurements

Electrochemical measurements were conducted on the workstation (CHI 760E, CHI 1140C) with the as-synthesized electrodes, Hg/HgO, and graphite rod as the working electrode, reference electrode, and counter electrode, respectively. The Ni-BDC/NF and the RuO_2/NF were activated by CV cycles at a scan rate of 50 mV s^{-1}. The reconstructed sample has already undergone the CV activation process, so there is no need to repeat this process. Linear sweep voltammetry (LSV) curves were scanned at 5 mV s^{-1}. The *iR* drop was corrected using the uncompensated series resistance. All the measured potentials were converted to reversible hydrogen electrodes (RHEs): $E_{RHE} = E_{Hg/HgO} + 0.0592 \times pH + 0.098$ (V).

3 Results and discussion

A continuous Fe^{3+} releasing enabled complete reconstruction strategy is proposed in this study to promote the conversion of Ni-BDC into Fe-doped nickel hydroxide/oxyhydroxide (Fe-$NiO_x(OH)_y$) (Figure 1a). Briefly, Ni foam supported Ni-BDC nanosheet arrays (Ni-BDC/NF) were prepared *via* a simple solvothermal method [22,23]. The morphology and phase of the powder collected from Ni-BDC/NF are essentially identical to the Ni-BDC growing on the Ni foam (Figure S1a–c, Supporting Information online). The Ni-BDC

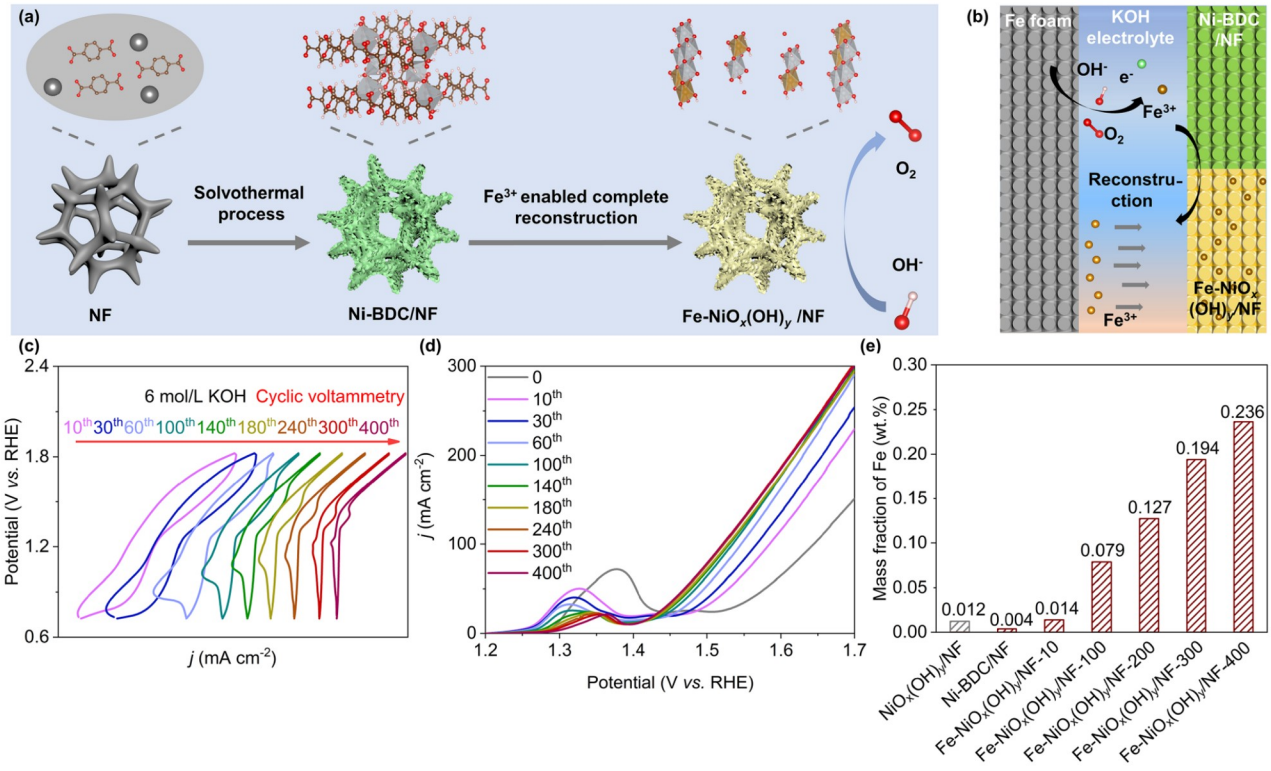

Figure 1 (a) Scheme for the synthesis of Fe-$NiO_x(OH)_y$/NF. (b) Schematic diagram of continuous Fe^{3+} releasing enabled complete reconstruction of Ni-BDC. (c) CV curves collected during the reconstruction of Ni-BDC/NF to form Fe-$NiO_x(OH)_y$/NF (without *iR* correction). (d) LSV curves of Ni-BDC/NF reconstructed with different CV cycles (Fe-$NiO_x(OH)_y$/NF-*z*) in 6.0 M KOH at 5 mV s^{-1} (without *iR* correction). (e) Fe contents of Ni-BDC/NF and the reconstructed samples (color online).

nanosheet arrays with high crystallinity are composed of uniformly distributed C, O, and Ni, as confirmed by transmission electron microscopy (TEM), selected area electron diffraction (SAED), and energy-dispersive X-ray (EDX) spectra (Figure S2). Then, the reconstruction of Ni-BDC/NF was initiated by CV in high-concentration KOH solution (6.0 M) and the *in situ* Fe^{3+} doping was realized by the continuous releasing of Fe^{3+} from the Fe foam counter electrode during CV activation. The working electrode, Ni-BDC/NF, is unstable in high-concentration KOH solution [24,25]. The hydrolysis of Ni-BDC leads to Ni^{2+} leaching and the destruction of metal-ligand coordination [24]. With the continuous releasing of Fe^{3+} from the Fe foam counter electrode (Figure S3), the Ni-BDC/NF is completely reconstructed into Fe-$NiO_x(OH)_y$/NF after 300 CV cycles (Figure 1a, b). By replacing the Fe foam counter electrode with graphite rod, an Fe-free catalyst ($NiO_x(OH)_y$/NF) is obtained.

CV activation was used to convert the Ni-BDC/NF precursor into Fe-$NiO_x(OH)_y$/NF. A pair of redox peaks can be observed in the CV profiles, which is from the oxidation/reduction of Ni species (Figure 1c). The redox peaks undergo a continuous decrease in intensity with cycling due to the leaching of nickel ions from the Ni-BDC/NF [26]. The CV profiles gradually stabilize after 300 CV cycles (Figure 1c), suggesting the complete of reconstruction. Notably, when the Fe foam is replaced by a graphite rod, the decreasing trend in redox peak intensity is somewhat weakened, highlighting the crucial role of Fe^{3+} (*in situ* released from the Fe foam) in promoting the reconstruction process (Figure S4a).

The effect of KOH concentration on the reconstruction process is studied by tuning the KOH concentration from 1.0 to 8.0 M (Figure S4b–d). Generally, the higher the KOH concentration, the greater decrease in redox peak intensity during CV activation. Especially, with a low KOH concentration (1.0 M), the redox peaks do not shrink significantly during CV activation (Figure S4b), indicating that the reconstruction of Ni-BDC/NF is enhanced in high-concentration KOH solution.

The OER activity in high-concentration KOH solution is of crucial importance for industrial applications. Thus, LSV was performed for the reconstructed samples in 6.0 M KOH (Figure 1d). Generally, the OER activity of the sample increases with the CV activation number, and remains stable after 300 cycles (the LSV curve of the sample reconstructed after 400 CV cycles overlaps with that after 300 CV cycles). The potential at 100 mA cm^{-2} gradually decreases from 0 to 300 CV cycles and then remains stable (Figure S5a). With the increase of CV activation number from 0 to 100, the area of the oxidation peak decreases continuously (Figure S5b).

After 100 CV cycles, the oxidation peak shows an obvious tendency to move towards positive potential. The continuous introduction of Fe^{3+} in the reconstructed catalyst is responsible for the gradual improvement of catalytic activity with CV activation number [27,28]. The shrinking of the large oxidation peak makes this trend difficult to be observed in the first 100 cycles.

To explore the relationship between the Fe-doping amount and CV activation number, inductively coupled plasma (ICP) was conducted. The mass fraction of Fe in $NiO_x(OH)_y$/NF, Ni-BDC/NF, Fe-$NiO_x(OH)_y$/NF-10, Fe-$NiO_x(OH)_y$/NF-100, Fe-$NiO_x(OH)_y$/NF-200, Fe-$NiO_x(OH)_y$/NF-300, and Fe-$NiO_x(OH)_y$/NF-400 are 0.012, 0.004, 0.014, 0.079, 0.127, 0.194, and 0.236 wt.%, respectively (Figure 1e). The trace amount of Fe in $NiO_x(OH)_y$/NF prepared with a graphite rod counter electrode is mainly derived from Fe impurity in KOH solution [29], and the Fe content of Fe-$NiO_x(OH)_y$/NF-300 is much higher than that of $NiO_x(OH)_y$/NF. The ICP results indicate that both the Fe foam counter electrode and high-concentration KOH solution play significant roles in Fe doping. Moreover, there is a quasi-linear relationship between the Fe-doping amount and the CV activation number within 300 cycles. To determine the Fe content in Fe-$NiO_x(OH)_y$ (without the Ni foam substrate), the powder grown on NF is detached from Fe-$NiO_x(OH)_y$/NF and analyzed by ICP. The mass fractions of Ni and Fe are 45.8 and 3.8 wt.%, respectively, and the Ni/Fe mass ratio is ~12:1 (Figure S6).

To investigate the structure and valence state evolution during the conversion of Ni-BDC/NF to Fe-$NiO_x(OH)_y$/NF, *in situ* Raman, *ex situ* X-ray diffraction (XRD), and X-ray photoelectron spectroscopy (XPS) were performed. When the Ni-BDC/NF is immersed in 6.0 M KOH without CV cycling (0), the Raman peaks corresponding to Ni-BDC shrink or disappear, while new peaks from α-$Ni(OH)_2$ emerge at 450, 3,610, and 3,665 cm^{-1} (Figure 2a, b) [28,30,31]. The Raman results indicate that a portion of Ni-BDC is converted into α-$Ni(OH)_2$ by immersing in 6.0 M KOH.

Drastic change in Raman spectra can be observed in the first 10 CV cycles. The emergence of new peaks at 474 (Ni-O bending vibration, δ mode) and 554 cm^{-1} (Ni–O stretching vibration, ν mode) suggests the formation of γ-NiOOH [32–34] (Figure 2a). The disappearance of the 450 cm^{-1} peak associated with α-$Ni(OH)_2$ is due to the overlap with the strong NiOOH Raman band. The peaks at 630, 858, 1,130, 1,420, and 1,611 cm^{-1} from the H_2BDC ligand of Ni-BDC experience a gradual decrease in intensity and eventual disappearance [35,36]. The weak peak at 3,581 cm^{-1} suggests the possible formation of β-$Ni(OH)_2$ (Figure 2b) [30]. The emergence of this peak is caused by the aging of α-$Ni(OH)_2$ and its transformation into β-$Ni(OH)_2$ [29]. During this period, the reconstruction mainly involves the phase transition of Ni-BDC into nickel hydroxide/oxyhydroxide, while the *in situ* Fe doping is negligible (Figure 1e). With the increase of cycle number to 20, the Raman peaks from the H_2BDC ligand disappear completely. This indicates that the surface Ni-BDC is completely transformed into nickel hydroxide/oxyhydroxide. The Raman band at 3,581 cm^{-1} disappears, which may be caused by the *in situ* Fe doping inhibited production of β-$Ni(OH)_2$.

With the proceeding of CV cycle number from 20 to 300, no new peaks are observed in the Raman spectra. Nevertheless, the continuous introduction of Fe^{3+} in the sample causes the gradual decrease in peak area ratio of Ni–O δ-mode to ν-mode (δ/ν) from 2.13 to 1.45 (Figures S7 and S8). The δ/ν ratio is regarded as a descriptor for the disorder degree [32,37]. The smaller the I_δ/I_ν ratio, the greater the disorder degree. This indicates that the Fe^{3+} doping in the γ-NiOOH lattice results in lattice mismatch and thus structural defects [32,37,38]. Compared to the Fe-$NiO_x(OH)_y$/NF prepared with the Fe foam counter electrode, the $NiO_x(OH)_y$/NF prepared with the graphite counter electrode presents a much higher I_δ/I_ν ratio (2.35 *vs.* 1.45) (Figure S9). The results suggest that the *in situ* Fe^{3+} doping caused by the continuous releasing of Fe^{3+} from Fe foam would exacerbate the reconstruction of Ni-BDC by introducing more defects in the reconstructed catalyst, possibly bringing more active sites and thus better OER catalytic activity.

To further analyze the impact of Fe^{3+} doping on the reconstruction of Ni-BDC/NF, the reconstructed samples were analyzed with XPS. After CV activation, a substantial amount of C is leached away from the Ni-BDC/NF, while the Ni and Fe contents increase (Figure 2c). The O 1s spectrum of Ni-BDC/NF shows two peaks at 531.7 eV (O1) and 533.2 eV (O2), which can be assigned to the carboxylate groups of H_2BDC and absorbed water, respectively [39,40]. After CV activation, the O 1s spectra show three components at 529.2 eV (O3), 531.1 eV (O4), and 532.7 eV (O5), which are from the metal-oxygen bonds, defects, and surface-adsorbed oxygen species, respectively [41–43] (Figure 2d). Moreover, the existence of oxygen vacancies of the reconstructed catalyst (Fe-$NiO_x(OH)_y$/NF) has been further confirmed by electron paramagnetic resonance (EPR, Figure S10a). This indicates that the CV activation decomposes the metal-ligand coordination, leading to the appearance of abundant oxygen vacancies and defects during the reconstruction [24]. With increasing CV number, the O 1s peak shifts towards higher binding energy, and the O4 component becomes more dominant, which is related to the formation of nickel hydroxide/oxyhydroxide and *in situ* Fe^{3+} doping [43].

The Ni 2p XPS spectrum of Ni-BDC/NF exhibits two major peaks at 856.1 (Ni $2p_{3/2}$) and 873.8 eV (Ni $2p_{1/2}$) with corresponding satellite peaks [44,45] (Figure 2e). After CV activation, the two major peaks from Ni(II) shift to lower binding energies (Ni $2p_{3/2}$ at 855.5 eV, Ni $2p_{1/2}$ at 873.1 eV). This is caused by the conversion of Ni-BDC to nickel hy-

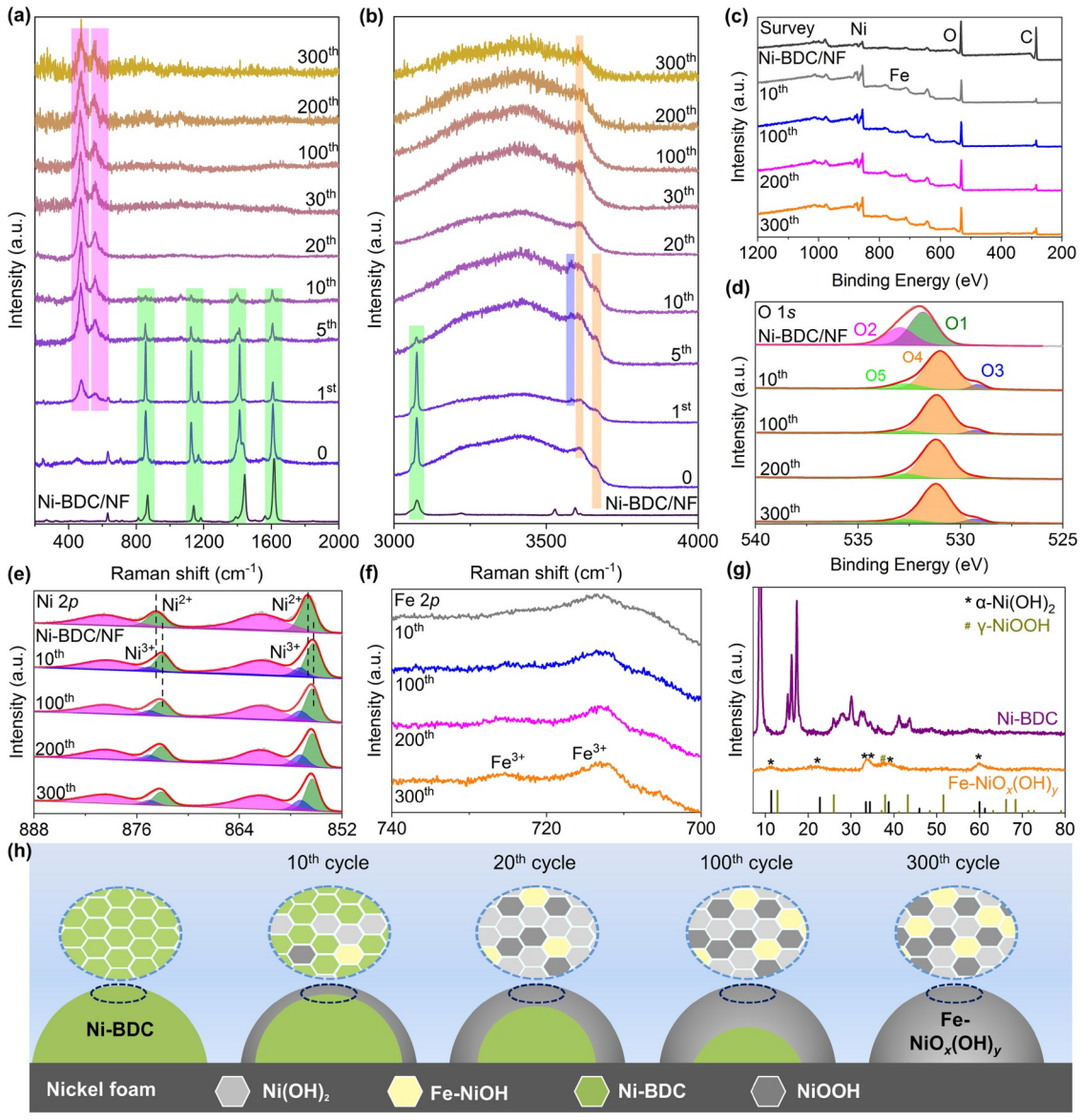

Figure 2 *In situ* Raman spectra of Ni-BDC/NF during the reconstruction (a) in the range of 200–2,000 cm^{-1} and (b) 3,000–4,000 cm^{-1}. XPS spectra of Ni-BDC/NF and the reconstructed samples (Fe-$NiO_x(OH)_y$/NF-*z*): (c) survey spectra, (d) O 1s spectra, (e) Ni 2p spectra, and (f) Fe 2p spectra. (g) XRD patterns of Ni-BDC and Fe-$NiO_x(OH)_y$. (h) Schematic reconstruction process of Ni-BDC/NF (color online).

droxide with increased local electron density and thus reduced binding energy [46]. Additionally, two new components emerge at 856.9 (Ni $2p_{3/2}$) and 874.5 eV (Ni $2p_{1/2}$), suggesting the formation of Ni(III) [46]. Interestingly, the increase of CV cycle number results in a positive shift for the Ni (II) 2p major peaks [39]. The above-mentioned changes in the XPS spectra mainly occur in the first 100 cycles, as the catalyst's surface has undergone complete reconstruction in the first 100 cycles. Compared to the $NiO_x(OH)_y$/NF, the major O 1s and Ni 2p peaks of Fe-$NiO_x(OH)_y$/NF shift positively, which is caused by the Fe doping (Figure S10b, c). The Fe 2p spectra show relatively weak and broad peaks at ~713.0 (Fe $2p_{3/2}$) and 725.4 eV (Fe $2p_{1/2}$), suggesting the +3 oxidation state of Fe in the reconstructed samples (Figure 2f) [21].

To further determine the phase of the reconstructed catalyst, the Ni-BDC/NF and Fe-$NiO_x(OH)_y$/NF were subjected to sonication and the powders grown on the Ni foam were collected for XRD analysis. XRD (Figure 2g) demonstrates that the Ni-BDC with high crystallinity is transformed into a mixture of α-$Ni(OH)_2$ (00-038-0715) [47,48] and γ-NiOOH (00-006-0075) [49] with low crystallinity after 300 CV cycles. The Fe exists in the Fe-$NiO_x(OH)_y$/NF by replacing the Ni atoms in the lattice of $Ni(OH)_2$/NiOOH.

According to the above results, the phase and composition evolution of Ni-BDC/NF during the reconstruction process are schematically shown in Figure 2h. The Ni-BDC/NF precursor is unstable in high-concentration KOH. It under-

goes hydrolysis and is initially converted into $Ni(OH)_2$. During the CV activation, a portion of $Ni(OH)_2$ is oxidized into NiOOH under high anode potential. Meanwhile, the incorporation of Fe^{3+} in $Ni(OH)_2$/NiOOH leads to lattice mismatch and defects. After 20 CV cycles, the Ni-BDC on the surface has been completely transformed into Fe-doped $Ni(OH)_2$/NiOOH. With the increase of CV cycles, the depth of reconstruction increases, accompanied by the continuous incorporation of Fe^{3+}. After 300 CV cycles, the Ni-BDC grown on Ni foam is completely transformed into Fe-$NiO_x(OH)_y$.

The morphology of Fe-$NiO_x(OH)_y$ was characterized by scanning electron microscopy (SEM) and atomic force microscopy (AFM). Although the Ni-BDC undergoes structural reconstruction during CV activation, the as-synthesized Fe-$NiO_x(OH)_y$ after 300 CV cycles generally inherit the nanosheet morphology of Ni-BDC, even after cycling (Figure 3a, b, Figure S11). Despite this fact, the gradual collapse of nanosheets can still be observed during the reconstruction process (Figure S11). AFM topological image (Figure 3c) shows that the Fe-$NiO_x(OH)_y$ nanosheet has an ultrathin thickness of only 2.2 nm, which is thinner than that of Ni-BDC (~3.6 nm) and $NiO_x(OH)_y$ (~3.0 nm) nanosheets (Figure S12).

TEM confirms the ultrathin nanosheet structure of Fe-$NiO_x(OH)_y$ (Figure 3d). The SAED (Figure 3e) pattern exhibits three weak and continuous diffraction rings from α-$Ni(OH)_2$ and another diffraction ring from γ-NiOOH. High-angle annular dark-field scanning TEM (HAADF-STEM) reveals that the Fe-$NiO_x(OH)_y$ nanosheet consists of numerous fine domains with low crystallinity (Figure 3f). In addition, the (113) lattice fringe of α-$Ni(OH)_2$ and the (10-5) and (015) lattice fringes of γ-NiOOH can be clearly observed in the high-resolution HAADF-STEM image. The HADDF-STEM image and corresponding EDX mapping (Figure 3g) reveal the even distribution of Fe, Ni, O, and C in Fe-$NiO_x(OH)_y$, which also demonstrates the successful introduction of Fe. Based on the above characterizations, it can be concluded that the Ni-BDC is completely reconstructed into α-$Ni(OH)_2$/γ-NiOOH heterogeneous ultrathin nanosheets with low crystallinity during CV activation.

The as-prepared samples grown on Ni foam were used as the working electrodes for OER performance evaluation in a three-electrode system. Compared to the Ni-BDC/NF, the

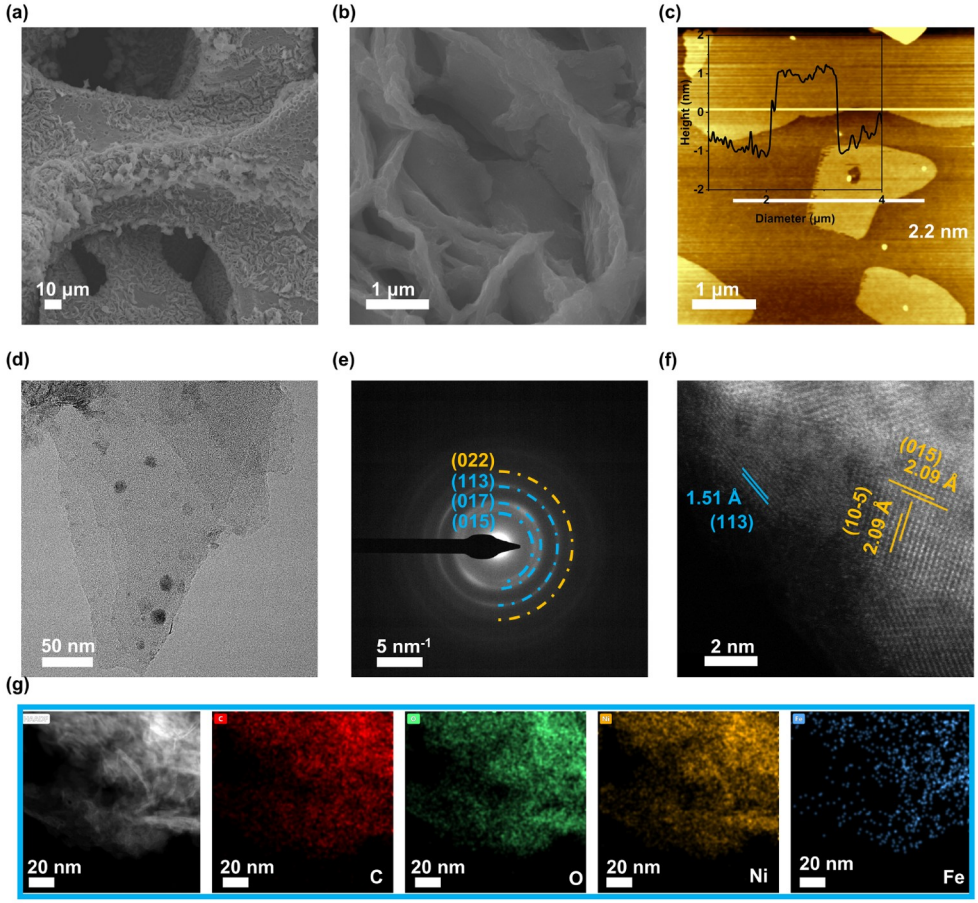

Figure 3 (a, b) SEM images of Fe-$NiO_x(OH)_y$/NF. (c) AFM topological image (inset: height profile of a single-layer nanosheet along the white line) of Fe-$NiO_x(OH)_y$. (d) TEM image of Fe-$NiO_x(OH)_y$ and (e) the corresponding SAED pattern. (f) HAADF-STEM image of Fe-$NiO_x(OH)_y$. (g) HAADF-STEM image and the corresponding EDX mappings of Fe-$NiO_x(OH)_y$ (color online).

reconstructed catalysts show significantly smaller redox peaks (Figure S13). In addition, the *in situ* Fe doping and the increase of KOH concentration further reduce the redox peak area. At 10 and 100 mA cm^{-2}, the overpotential of Fe-$NiO_x(OH)_y$/NF are 217 and 263 mV, respectively (Figure 4a). The overpotentials of Fe-$NiO_x(OH)_y$/NF are significantly smaller than those of Ni-BDC/NF (286, 365 mV), $NiO_x(OH)_y$/NF (279, 342 mV), Fe-$NiO_x(OH)_y$/NF-4M (229, 280 mV), Fe-$NiO_x(OH)_y$/NF-8M (262, 315 mV), and RuO_2/NF (304, 381 mV). Tafel slope is used to reflect the reaction kinetics of the OER catalysts. The Tafel slopes of Fe-$NiO_x(OH)_y$/NF, Ni-BDC/NF, $NiO_x(OH)_y$/NF, Fe-$NiO_x(OH)_y$/NF-4M, Fe-$NiO_x(OH)_y$/NF-8M, and RuO_2/NF are determined to be 44.9, 78.7, 62.1, 53.1, 51.9, and 76.6 mV dec^{-1} (Figure 4b), respectively. The Fe-$NiO_x(OH)_y$/NF shows the lowest Tafel slope, corresponding to the fastest reaction kinetics. In addition, the OER performances of catalysts obtained by the reconstitution of Ni-BDC/NF in 1.0 M KOH (Fe-$NiO_x(OH)_y$/NF-1M) and the reconstruction of pure Ni foam in 6.0 M KOH (Fe-NF) are evaluated. The Fe-$NiO_x(OH)_y$/NF manifests much lower overpotential and Tafel slope than the Fe-$NiO_x(OH)_y$/NF-1M and Fe-NF (Figure S14), demonstrating the significant role of both high concentration KOH and Ni-BDC precursor in obtaining high-performance OER catalyst. The required overpotential at 10 mA cm^{-2} and Tafel slope of Fe-$NiO_x(OH)_y$/NF-100, Fe-$NiO_x(OH)_y$/NF-200 and Fe-$NiO_x(OH)_y$/NF catalysts are decreasing, indicating that the OER performance of the catalyst is improving as CV reconstruction proceeds. Moreover, Fe-$NiO_x(OH)_y$/NF demonstrates superior OER performance compared to similar reported catalysts (Table S1, Supporting Information online). The turnover frequency (TOF) of Fe-$NiO_x(OH)_y$/NF at an over-

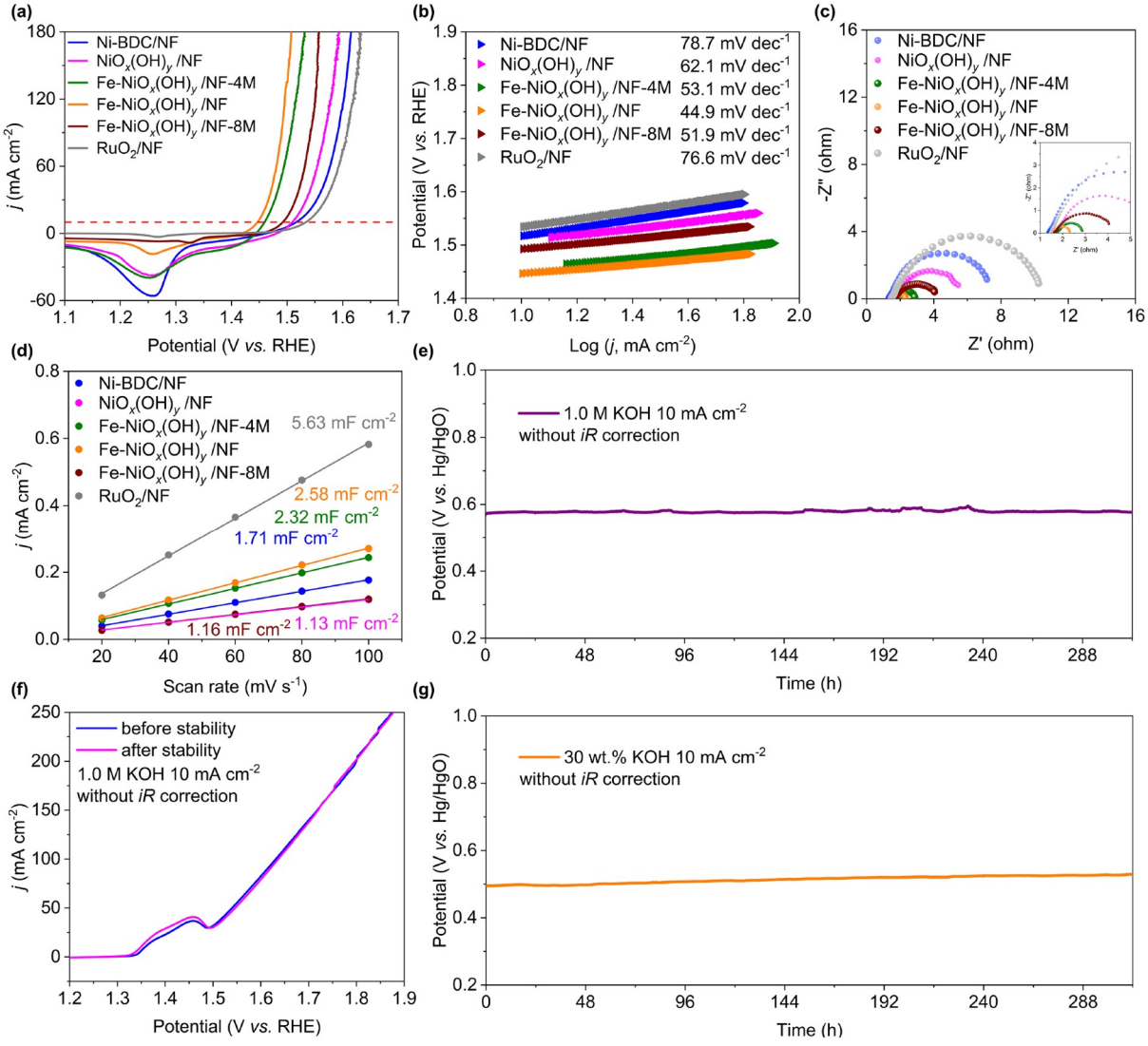

Figure 4 (a) LSV curves of Ni-BDC/NF, $NiO_x(OH)_y$/NF, Fe-$NiO_x(OH)_y$/NF-4M, Fe-$NiO_x(OH)_y$/NF, Fe-$NiO_x(OH)_y$/NF-8M, and RuO_2/NF in 1.0 M KOH at 5 mV s^{-1}. (b) Tafel plots of different catalysts. (c) The Nyquist plots of different catalysts. (d) CV current density *versus* scan rate and the linear slope is equal to the C_{dl}. (e) Durability of Fe-$NiO_x(OH)_y$/NF in 1.0 M KOH (5.3 wt.%) at 10 mA cm^{-2} (without *iR* correction). (f) LSV curves of Fe-$NiO_x(OH)_y$/NF before and after durability test (without *iR* correction). (g) Durability of Fe-$NiO_x(OH)_y$/NF in 30 wt.% KOH at 10 mA cm^{-2} (without *iR* correction) (color online).

potential of 300 mV is calculated to be 0.11 s^{-1}, significantly surpassing that of Ni-BDC/NF (0.003 s^{-1}). It suggests the reaction kinetics on a single active site of the catalyst has been greatly improved after reconstruction.

Electrochemical impedance spectroscopy (EIS) was conducted to illustrate the charge transfer ability of the catalysts. The Fe-$NiO_x(OH)_y$/NF exhibits the lowest charge transfer resistance (R_{ct}) of 0.87 Ω among the samples (Figure 4c). The R_{ct} of Ni-BDC/NF, $NiO_x(OH)_y$/NF, Fe-$NiO_x(OH)_y$/NF-4M, Fe-$NiO_x(OH)_y$/NF-8M, and RuO_2/NF are 6.57, 4.25, 1.17, 2.67, and 9.29 Ω, respectively. The EIS results indicate that both CV activation in high-concentration KOH and *in situ* Fe doping improve the charge transfer ability of the sample.

Electrochemically active surface area (ECSA) can be estimated from the double-layer capacitance (C_{dl}), which is calculated from the non-Faraday potential regions of CV profiles (Figure S15). The C_{dl} of Fe-$NiO_x(OH)_y$/NF, Ni-BDC/NF, $NiO_x(OH)_y$/NF, Fe-$NiO_x(OH)_y$/NF-4M, Fe-$NiO_x(OH)_y$/NF-8M, and RuO_2/NF are determined to 2.58, 1.71, 1.13, 2.32, 1.16, and 5.63 mF cm^{-2} (Figure 4d), respectively. The Fe-$NiO_x(OH)_y$/NF shows a relatively high C_{dl} value, indicating its relatively large ESCA. Usually, a large ECSA means a large electrolyte/electrode contact interface and it would lead to more exposed active sites. It should be mentioned that the RuO_2/NF exhibits a larger C_{dl} but lower OER activity than the Fe-$NiO_x(OH)_y$/NF. This is because the C_{dl} can be used to reflect the exposed ECSA of catalysts, but it is not necessarily positively correlated with the OER activity [44]. To show the intrinsic OER activity of the samples, LSV curves and Tafel plots normalized by ECSA are provided in Figure S16. After normalization, the Fe-$NiO_x(OH)_y$/NF still manifests the smallest overpotential (234 mV at 10 mA cm^{-2}) and lowest Tafel slope (50.3 mV dec^{-1}).

The long-term stability of Fe-$NiO_x(OH)_y$/NF was tested in both 1.0 M (Figure 4e, f) and 30 wt.% KOH (Figure 4g) at 10 mA cm^{-2} by chronopotentiometry. The Fe-$NiO_x(OH)_y$/NF exhibits ignorable activity decay (0.03 mV h^{-1} for 312 h) during the stability test in 1.0 M KOH as can be reflected from the overlapping of LSV curves before and after stability test (Figure 4e, f). Moreover, the Fe-$NiO_x(OH)_y$/NF can work stably (activity decay: 0.1 mV h^{-1}) and continuously for more than 312 h even under industrial alkaline conditions (30 wt.% KOH, Figure 4g). *Ex situ* Raman and XPS were employed to explore the phase and electronic structure evolution of the catalyst. Raman spectra collected after the stability test show no obvious change in peak position and $I_δ/I_v$ value, demonstrating the excellent stability of Fe-$NiO_x(OH)_y$/NF. In addition, the XPS spectra show insignificant change in chemical composition and surface valence state (Figure S17), further confirming the ideal stability of the catalyst. Even at 100 mA cm^{-2}, the Fe-$NiO_x(OH)_y$/NF is able to work continuously for 200 h with a slow activity decay of 0.09 mV h^{-1} under industrial alkaline conditions (30 wt.% KOH, Figure S18).

4 Conclusions

In summary, an Fe-doped nickel hydroxide/oxyhydroxide (Fe-$NiO_x(OH)_y$/NF) OER electrocatalyst with low crystallinity and abundant defects has been constructed by the electrochemical reconstruction of Ni-BDC/NF in 6.0 M KOH. The continuous releasing of Fe^{3+} from the Fe foam counter electrode enables the *in situ* doping of Fe^{3+} and creates abundant defects in the reconstructed catalyst, which accelerates the reconstruction process and enhances the OER activity. The Fe-$NiO_x(OH)_y$/NF manifests decent OER performance in terms of overpotential and stability in both 1.0 M KOH and industrial alkaline conditions (30 wt.% KOH), showing great potential for industrial water electrolysis.

Acknowledgements This work was supported by the China Postdoctoral Science Foundation (2022T150502) and the National Energy-Saving and Low-Carbon Materials Production and Application Demonstration Platform Program (TC220H06N).

Conflict of interest The authors declare no conflict of interest.

Supporting information The supporting information is available online at http://chem.scichina.com and http://link.springer.com/journal/11426. The supporting materials are published as submitted, without typesetting or editing. The responsibility for scientific accuracy and content remains entirely with the authors.

1 Wan S, Xu J, Cao S, Yu J. *Interdisciplinary Mater*, 2022, 1: 294–308
2 Hu S, Wang S, Feng C, Wu H, Zhang J, Mei H. *ACS Sustain Chem Eng*, 2020, 8: 7414–7422
3 Ao K, Wei Q, Daoud WA. *ACS Appl Mater Interfaces*, 2020, 12: 33595–33602
4 Wang K, Liang C, Li S, Li J, Yi Z, Xu F, Wang Y, Lei L, Zhu M, Li S, Zhuang L, Xu Z. *Sci China Mater*, 2023, 66: 2662–2671
5 Bhanja P, Kim Y, Paul B, Kaneti YV, Alothman AA, Bhaumik A, Yamauchi Y. *Chem Eng J*, 2021, 405: 126803
6 Bhanja P, Kim Y, Paul B, Lin J, Alshehri SM, Ahamad T, Kaneti YV, Bhaumik A, Yamauchi Y. *ChemCatChem*, 2020, 12: 2091–2096
7 Böhm D, Beetz M, Schuster M, Peters K, Hufnagel AG, Döblinger M, Böller B, Bein T, Fattakhova-Rohlfing D. *Adv Funct Mater*, 2020, 30: 1906670
8 Li W, Feng B, Yi L, Li J, Hu W. *ChemSusChem*, 2021, 14: 730–737
9 Guo Y, Zhang C, Zhang J, Dastafkan K, Wang K, Zhao C, Shi Z. *ACS Sustain Chem Eng*, 2021, 9: 2047–2056
10 Lu J, Liu Y, Liang HP. *Sci China Chem*, 2023, 67: 687
11 Zhang R, Wu Q, Sherrell P, Li D, Huang K, Chen J, Yao X. *Sci China Chem*, 2023, 66: 2221–2237
12 Septiani NLW, Kaneti YV, Fathoni KB, Guo Y, Ide Y, Yuliarto B, Jiang X, Nugraha X, Dipojono HK, Golberg D, Yamauchi Y. *J Mater Chem A*, 2020, 8: 3035–3047
13 Seenivasan S, Seo J. *Chem Eng J*, 2023, 454: 140558
14 Hua W, Sun H, Li Y, Zhang Y, Wang JG. *Energy Mater Devices*, 2023, 1: 9370014
15 Huang C, Zhou Q, Duan D, Yu L, Zhang W, Wang Z, Liu J, Peng B,

An P, Zhang J, Li L, Yu J, Yu Y. *Energy Environ Sci*, 2022, 15: 4647–4658
16 Fang Y, Fang Y, Zong R, Yu Z, Tao Y, Shao J. *J Mater Chem A*, 2022, 10: 1369–1379
17 Wu T, Sun Y, Ren X, Wang J, Song J, Pan Y, Mu Y, Zhang J, Cheng Q, Xian G, Xi S, Shen C, Gao HJ, Fisher AC, Sherburne MP, Du Y, Ager JW, Gracia J, Yang H, Zeng L, Xu ZJ. *Adv Mater*, 2023, 35: 2207041
18 Dai W, Bai X, Zhu Y, Zhang Y, Lu T, Pan Y, Wang J. *J Mater Chem A*, 2021, 9: 6432–6441
19 Zhang J, Ye Y, Wei B, Hu F, Sui L, Xiao H, Gui L, Sun J, He B, Zhao L. *Appl Catal B-Environ*, 2023, 330: 122661
20 Ding J, Fan T, Shen K, Li Y. *Appl Catal B-Environ*, 2021, 292: 120174
21 Li CF, Tang HB, Zhao JW, Li GR. *J Mater Chem A*, 2023, 11: 5841–5850
22 Dong Q, Shuai C, Mo Z, Guo R, Liu N, Liu G, Wang J, Liu W, Chen Y, Liu J, Jiang Y, Gao Q. *CrystEngComm*, 2021, 23: 1172–1180
23 Liu Q, Xie L, Shi X, Du G, Asiri AM, Luo Y, Sun X. *Inorg Chem Front*, 2018, 5: 1570–1574
24 Singh B, Yadav A, Indra A. *J Mater Chem A*, 2022, 10: 3843–3868
25 Zheng W, Lee LYS. *ACS Energy Lett*, 2021, 6: 2838–2843
26 Guan D, Ryu G, Hu Z, Zhou J, Dong CL, Huang YC, Zhang K, Zhong Y, Komarek AC, Zhu M, Wu X, Pao CW, Chang CK, Lin HJ, Chen CT, Zhou W, Shao Z. *Nat Commun*, 2020, 11: 3376
27 Anantharaj S, Kundu S, Noda S. *Nano Energy*, 2021, 80: 105514
28 Klaus S, Louie MW, Trotochaud L, Bell AT. *J Phys Chem C*, 2015, 119: 18303–18316
29 Trotochaud L, Young SL, Ranney JK, Boettcher SW. *J Am Chem Soc*, 2014, 136: 6744–6753
30 Hall DS, Lockwood DJ, Poirier S, Bock C, MacDougall BR. *ACS Appl Mater Interfaces*, 2014, 6: 3141–3149
31 Lo YL, Hwang BJ. *Langmuir*, 1998, 14: 944–950
32 Bai L, Lee S, Hu X. *Angew Chem Int Ed*, 2021, 60: 3095–3103
33 Chen D, Xiong X, Zhao B, Mahmoud MA, El-Sayed MA, Liu M. *Adv Sci*, 2016, 3: 1500433
34 Merrill M, Worsley M, Wittstock A, Biener J, Stadermann M. *J Electroanal Chem*, 2014, 717-718: 177–188
35 Li J, Huang W, Wang M, Xi S, Meng J, Zhao K, Jin J, Xu W, Wang Z, Liu X, Chen Q, Xu L, Liao X, Jiang Y, Owusu KA, Jiang B, Chen C, Fan D, Zhou L, Mai L. *ACS Energy Lett*, 2019, 4: 285–292
36 Sun F, Wang G, Ding Y, Wang C, Yuan B, Lin Y. *Adv Energy Mater*, 2018, 8: 1800584
37 Xu J, Wang BX, Lyu D, Wang T, Wang Z. *Int J Hydrogen Energy*, 2023, 48: 10724–10736
38 Lee S, Bai L, Hu X. *Angew Chem Int Ed*, 2020, 59: 8072–8077
39 Bo X, Hocking RK, Zhou S, Li Y, Chen X, Zhuang J, Du Y, Zhao C. *Energy Environ Sci*, 2020, 13: 4225–4237
40 Liu C, Wang J, Wan J, Cheng Y, Huang R, Zhang C, Hu W, Wei G, Yu C. *Angew Chem Int Ed*, 2020, 59: 3630–3637
41 Liu X, Guo R, Ni K, Xia F, Niu C, Wen B, Meng J, Wu P, Wu J, Wu X, Mai L. *Adv Mater*, 2020, 32: 2001136
42 Peng S, Gong F, Li L, Yu D, Ji D, Zhang T, Hu Z, Zhang Z, Chou S, Du Y, Ramakrishna S. *J Am Chem Soc*, 2018, 140: 13644–13653
43 Wang Y, Zhu Y, Zhao S, She S, Zhang F, Chen Y, Williams T, Gengenbach T, Zu L, Mao H, Zhou W, Shao Z, Wang H, Tang J, Zhao D, Selomulya C. *Matter*, 2020, 3: 2124–2137
44 Huang W, Chen C, Ling Z, Li J, Qu L, Zhu J, Yang W, Wang M, Owusu KA, Qin L, Zhou L, Mai L. *Chem Eng J*, 2021, 405: 126959
45 Rui K, Zhao G, Chen Y, Lin Y, Zhou Q, Chen J, Zhu J, Sun W, Huang W, Dou SX. *Adv Funct Mater*, 2018, 28: 1801554
46 Qian Q, Li Y, Liu Y, Yu L, Zhang G. *Adv Mater*, 2019, 31: 1901139
47 He S, Chen Y, Wang M, Nuomin H, Novello P, Li X, Zhu S, Liu J. *Nano Energy*, 2021, 80: 105528
48 Li J, Yao L, Wu D, King J, Chuang SSC, Liu B, Peng Z. *Appl Catal B-Environ*, 2022, 316: 121657
49 Kim B, Oh A, Kabiraz MK, Hong Y, Joo J, Baik H, Choi SI, Lee K. *ACS Appl Mater Interfaces*, 2018, 10: 10115–10122